



MATERIALS SCIENCE

Ultrastrong and ductile medium-entropy alloys via hierarchical ordering

Lei Gu^{1†}, Yonghao Zhao^{1,2,*†}, Yong Li¹, Rui Hou³, Fei Liang¹, Ruisheng Zhang¹, Yinxing Wu⁴, Yong Fan¹, Ningning Liang¹, Bing Zhou³, Yang Chen³, Gang Sha⁴, Guang Chen³, Yandong Wang⁵, Xiang Chen^{1*}

Long-range ordered phases in most high-entropy and medium-entropy alloys (HEAs/MEAs) exhibit poor ductility, stemming from their brittle nature of complex crystal structure with specific bonding state. Here, we propose a design strategy to severalfold strengthen a single-phase face-centered cubic (fcc) Ni₂CoFeV MEA by introducing trigonal κ and cubic L1₂ intermetallic phases via hierarchical ordering. The tri-phase MEA has an ultrahigh tensile strength exceeding 1.6 GPa and an outstanding ductility of 30% at room temperature, which surpasses the strength-ductility synergy of most reported HEAs/MEAs. The simultaneous activation of unusual dislocation multiple slip and stacking faults (SFs) in the κ phase, along with nano-SF networks, Lomer-Cottrell locks, and high-density dislocations in the coupled L1₂ and fcc phases, contributes to enhanced strain hardening and excellent ductility. This work offers a promising prototype to design super-strong and ductile structural materials by harnessing the hierarchical ordered phases.

INTRODUCTION

The emergence of high-entropy and medium-entropy alloys (HEAs/MEAs) with multi-principal elements inspires a surge of search for combinations of properties that differ from conventional alloy design (1–5). In general, the most studied single-phase face-centered cubic (fcc) HEAs/MEAs exhibit high ductility but often display low yield strength and ultimate tensile strength (UTS) (6–8). To substantially enhance their strength to the gigapascal-level, precipitate strengthening is the most effective strategy among the four classical strengthening methods, leveraging the intricate composition (9). Certain HEAs/MEAs strengthened with A₃B-type Ni₃Al L1₂ and AB-type NiAl B2 ordered nanoparticles exhibit excellent strength-ductility combinations (10–14). However, most precipitates resulting from disorder-to-order transition, such as D0₂₂, κ , and η , often lead to a substantial sacrifice of tensile ductility and, in some instances, brittleness (15–19). This is mainly attributed to the fact that long-range ordered (LRO) phases have lower crystal symmetry and stronger atomic bonding compared to their disordered counterparts.

The valence electron concentration (VEC), defined as the number of total electrons including the *d*-electrons accommodated in the valence band, constitutes a crucial physical parameter that dictates the crystal structures of ordered phases, and consequently influences mechanical properties (17, 20). Typically, the transition from the brittle tetragonal to trigonal and then to hexagonal ordered

structures, and finally to a ductile cubic ordered structure occurs gradually as the VEC decreases (15, 21, 22). For instance, in the Co-Fe-Ni-V alloy system, substituting Co with Ni in the hexagonal A₃B-type Co₃V ordered phase increases the VEC and thereby brings about the formation of the trigonal Co_{1.5}Ni_{1.5}V ordered phase, commonly referred to as the κ phase (23, 24). Conversely, replacing Co with Fe decreases the VEC, leading to the occurrence of the L1₂-type cubic ordered phase (24). In the equimolar CoFeNiV MEA, a single-phase L1₂ ordered structure emerges after a complete disorder-to-order transition, showcasing a high UTS of 1.1 GPa and good ductility of 20%, yet displaying a low yield strength of 380 MPa (25). Upon removal of Fe, the equimolar CoNiV MEA annealed below 800°C attains a nearly pure κ phase structure, resulting in substantially reduced strength (below 250 MPa) and extremely poor ductility less than 1% (16, 26, 27). In conclusion, the completely ordered MEAs are susceptible to intergranular embrittlement and exhibit low yield strengths at room temperature.

Here, we have devised an innovative strategy aimed at introducing the hierarchical ordered phases into a disordered fcc Ni₂CoFeV matrix through a two-step annealing process. The substantial addition of Ni serves two primary purposes: first, to stabilize the fcc phase, and second, to increase the overall VEC, thereby augmenting the driving force for the separation of the κ phase at intermediate temperatures. This results in a tri-phase structure composed of disordered fcc and ordered κ and L1₂ phases, culminating in the alloy with a gigapascal yield strength and an ultrahigh UTS exceeding 1.6 GPa, while maintaining an exceptional ductility of 30% at room temperature. The simultaneous activation of unusual deformation mechanisms contributes to enhanced strain hardening and excellent ductility.

RESULTS

Microstructures

A Ni₂CoFeV MEA with an actual composition of Ni_{38.6}Co_{20.2}Fe_{20.3}V_{20.9} (at %) was synthesized by vacuum induction melting. The ingot underwent multi-directional forging at room temperature and subsequent

¹Nano and Heterogeneous Materials Center, School of Materials Science and Engineering, Nanjing University of Science and Technology, Nanjing 210094, China.

²School of Materials Science and Engineering, Hohai University, Changzhou 213200, China.

³National Key Laboratory of Advanced Casting Technologies, MIIT Key Laboratory of Advanced Metallic and Intermetallic Materials Technology, Engineering Research Center of Materials Behavior and Design, Ministry of Education, Nanjing University of Science and Technology, Nanjing 210094, China. ⁴Herbert Gleiter Institute of Nanoscience, School of Materials Science and Engineering, Nanjing University of Science and Technology, Nanjing 210094, China. ⁵Beijing Advanced Innovation Center for Materials Genome Engineering, State Key Laboratory for Advanced Metals and Materials, University of Science and Technology Beijing, Beijing 100083, China.

*Corresponding author. Email: xiang.chen@njust.edu.cn (X.C.); yzhao@njust.edu.cn (Y.Z.)

†These authors contributed equally to this work.

homogenization at 1150°C. After homogenization treatment (HT), the sample exhibits a single-phase fcc structure with a lattice constant of 3.585 Å (Fig. 1A). All alloying elements are uniformly distributed, and no precipitate can be found in the HT alloy, which has an average grain size of ~90 μm (fig. S1). After cold rolling (CR), nanolamellar subgrains with high-density dislocations were produced in the elongated coarse grains and shear bands (fig. S2).

Subsequent recrystallization annealing (RA) at 750°C produced a heterogeneous grain structure, as shown in the backscattered electron (BSE) image (Fig. 1B). The RA alloy consists of micrometer- and submicrometer-sized near-equiaxed grains and lamellar grains, with the latter being a combination of annealing twins and κ phase (Fig. 1C). The near-equiaxed fcc grains display a wide grain size distribution ranging from 200 nm to 5.8 μm with an average grain size of ~1.5 μm and contains 94% high-angle grain boundaries (fig. S3). The growth of fcc grains is restricted by the presence of internal ultrafine lath-shaped κ phase. This κ phase suppresses the grain-boundary migration, resulting in the formation of near-equiaxed grains. The diffraction peak of κ phase with a trigonal structure (space group $R\bar{3}m$) is identified by x-ray diffraction (XRD), and the lattice constant of fcc phase decreased to 3.578 Å, as shown in Fig. 1A. The κ phase has an average equivalent circular diameter of ~530 nm, obtained from

electron backscattered diffraction (EBSD) data (fig. S3), and a volume fraction of ~13%, an average width of ~140 nm, and a length of ~1.3 μm, measured from transmission electron microscopy (TEM) images (Fig. 1D and fig. S4). The growth of most κ phase occurs from the grain boundaries throughout the entire grains, leading to an average length approximately equal to the average diameter of fcc grains. Some annealing-induced stacking faults (SFs) along {111} planes are observed in the fcc matrix (Fig. 1E). The κ phase growth is associated with the emission of typical $1/6\langle 112 \rangle$ Shockley partial dislocation on {111} planes, akin to the twinning process (28). This is confirmed by the coupled growth of annealing twin and κ phase (Fig. 1E). Figure 1F shows the emission of partial dislocations at the tip of κ phase coupled with fcc domains. The retaining nanoscale fcc lamellae lead to high-density SFs in the κ phase, as indicated by red arrows. Additionally, a 9R phase is detected in the fcc grain (fig. S5), formed by the emission of Shockley partials on every third {111} plane, featuring an abcacab stacking sequence (28). Figure 1G reveals the crystal structure of the fcc matrix combined with twin and κ phase. The orientation relationship between the κ phase and the fcc matrix is determined to be $(009)\kappa // (-11-1)fcc$ and $[010]\kappa // [011]fcc$, sharing the same {111} habit plane with the coherent boundary of the twin. Further confirmation is obtained by high-resolution

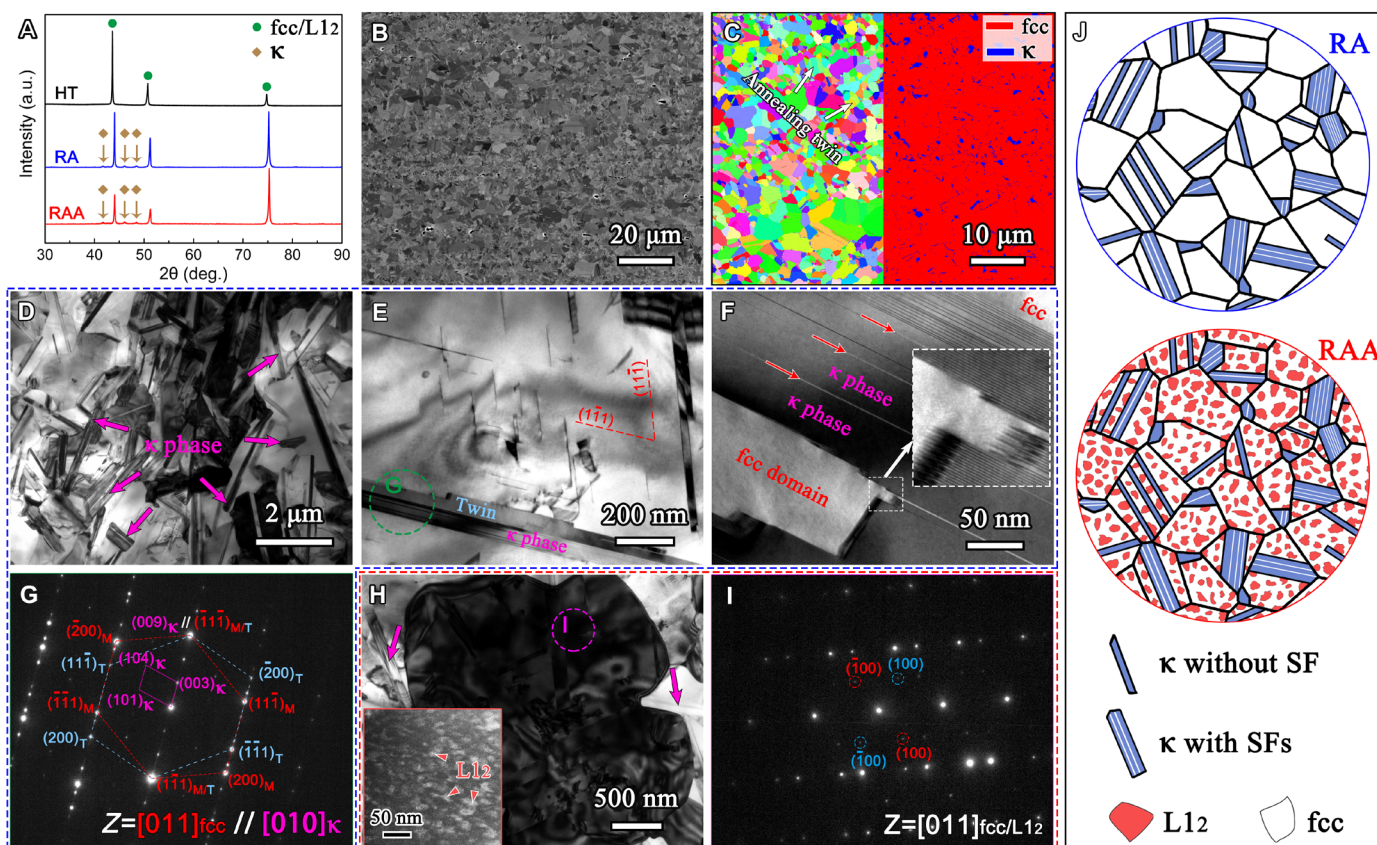


Fig. 1. Microstructural characterization and schematic diagram of Ni₂CoFeV MEA after thermomechanical treatment. (A) XRD patterns of the HT, RA, and RAA samples. (B) BSE image and (C) EBSD inverse pole figure and phase maps of the RA alloy. (D to F) Bright-field TEM images of the RA alloy showing plenty of ultrafine lath-shaped κ phase inside the fcc grains, pointed by pink arrows. The enlarged detail in (F) indicates the emission of partial dislocations at the tip of κ phase. (G) Selected-area electron diffraction (SAED) pattern of the circled area in (E) showing the crystal structures of κ and fcc with an annealing twin. (H) Bright-field TEM image and (I) SAED pattern of the RAA alloy revealing that disorder-to-order transition occurred in the fcc matrix. The inset in (H) shows the dark-field image of L₁₂ phase recorded from {100} superlattice spot. (J) Schematic diagrams of the hierarchical ordering process.

TEM (HRTEM) image and corresponding fast Fourier transform (FFT) patterns, as shown in fig. S6, revealing a coherent interface between the κ phase and the fcc phase, with an SF present in the κ phase. Scanning transmission electron microscopy (STEM) image and energy-dispersive spectroscopy (EDS) maps demonstrate that the κ phase is a distinct Fe-depleted region (fig. S7).

After further aging at 650°C (referred to as the RAA alloy), the fcc grains and κ phase hardly coarsen (fig. S3). Figure 1H shows that the RAA alloy also has numerous ultrafine lath-shaped κ phase inside the fcc grains and the growth of adjacent grains is impeded. Besides, a disorder-to-order transition occurs in the fcc matrix, leading to the formation of an ordered L_{12} structure. The dispersed and irregular white domains are the L_{12} phase, as shown in the inserted dark-field image (Fig. 1H). The coupled nanostructure comprises the interconnected disordered fcc matrix filled with discrete L_{12} ordered phase. These individually nucleated L_{12} domains in the fcc matrix do not coalesce. Therefore, thermal anti-phase boundaries (APBs) are not formed in the RAA alloy, which are observed in the fully ordered L_{12} CoFeNiV MEA (25). The existence of L_{12} phase is also verified by the presence of faint $\{100\}$ superlattice diffraction spots under the $[011]$ zone axis (Fig. 1I). However, there is no additional diffraction peak corresponding to L_{12} phase in the RAA alloy detected by XRD, due to its close similarity to the disordered fcc

phase. Nevertheless, the lattice constant of the fcc phase further decreases to 3.575 Å, indicating further precipitation in the fcc matrix. The absence of superlattice diffraction peaks in the XRD pattern can be attributed to the minor differences in constituent atoms (29). The schematic diagrams of the formation of the RAA alloy during the hierarchical ordering process are depicted in Fig. 1J. Figure 2A illustrates a κ phase formed adjacent to an annealing-induced nanotwin with a coherent boundary, maintaining an orientation relation of $(001)\kappa//[(1-11)fcc/L_{12}]$ and $[010]\kappa//[011]fcc/L_{12}$. The superlattice spots in the FFT pattern indicate that the nanotwin with an SF at the twin boundary has an LRO structure. Further analysis reveals that the coupled fcc/ L_{12} phases lack an obvious interface, yet their domains remain independent of each other (Fig. 2B). The L_{12} phase exhibits an orientation relation with the coherent fcc matrix as $(1-11)L_{12}//[1-11]fcc$ and $[011]L_{12}//[011]fcc$.

Atom probe tomography (APT) analyses were implemented to reveal the quantitative atomic-scale chemical composition of tri-phase RAA alloy. Figure 2C shows a typical reconstructed APT morphology with iso-composition surfaces of 20 at % Fe and 23 at % V, respectively. The lath-shaped κ phase exhibits a clear depletion in Fe but a slight enrichment in V and Co, with a composition of $Ni_{39}Co_{22.6}Fe_{14.5}V_{23.9}$ (at %) (Fig. 2D). This κ phase can be understood as a $(Co, Fe, Ni)_3V$ -type ordered structure with Fe replacing

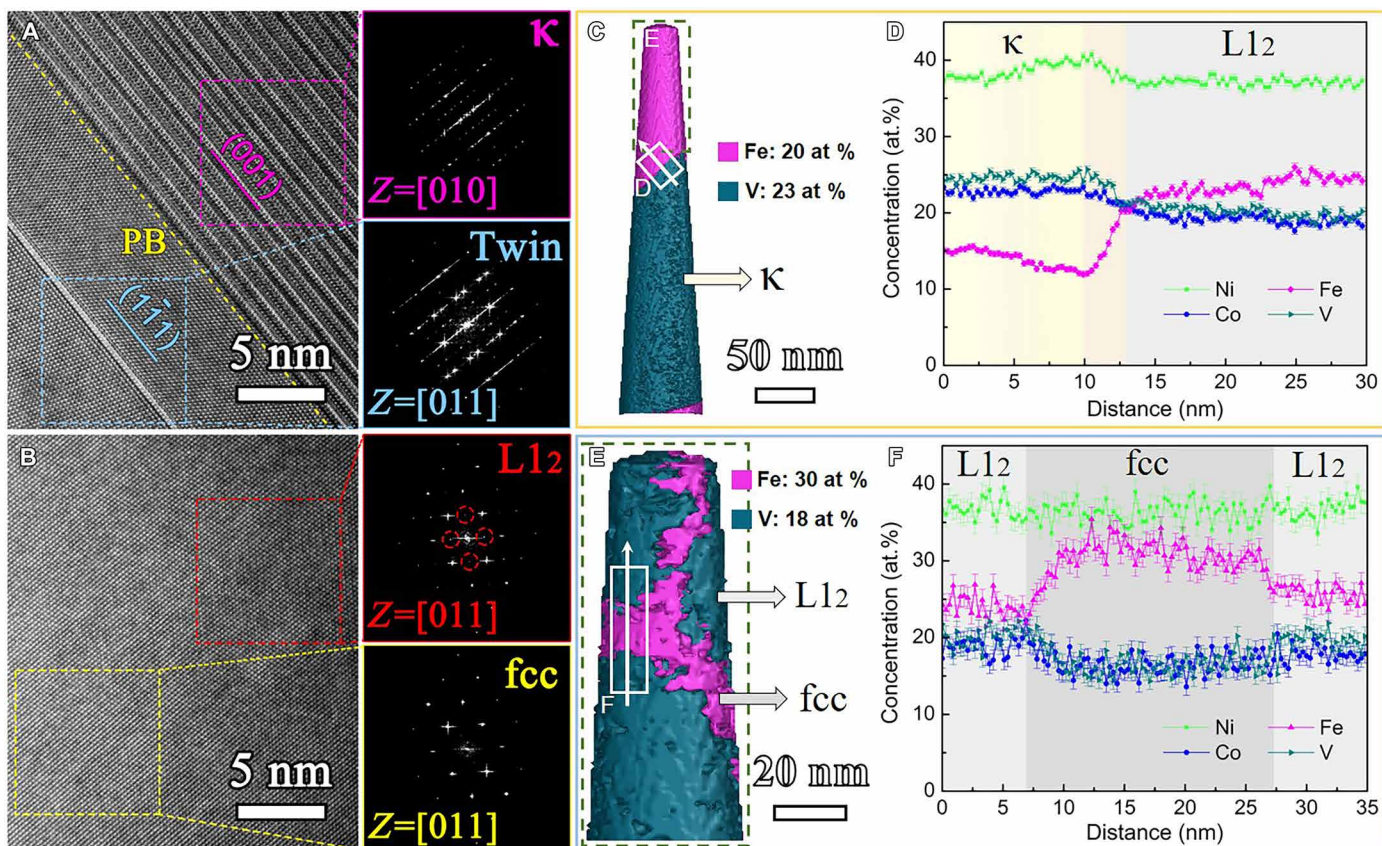


Fig. 2. Characterization of tri-phase structure comprising κ , L_{12} , and disordered fcc phases at the atomic scale. (A and B) HRTEM images and FFT patterns showing the atomic and crystal structures of κ , L_{12} , and fcc matrix, respectively. PB, phase boundary. APT three-dimensional reconstructions highlighted by iso-composition surfaces of (C) 20 at % Fe and 23 at % V and (E) 30 at % Fe and 18 at % V, presenting the morphologies of ordered κ and L_{12} phases and disordered fcc matrix. (D and F) One-dimensional concentration profiles showing the exact element distributions from κ to L_{12} and L_{12} to fcc and then to L_{12} .

Co in $\text{Co}_{1.5}\text{Ni}_{1.5}\text{V}$. The distributions of Co, Ni, and V in the κ phase are homogeneous at the nanoscale, while Fe exhibits minor fluctuations (see fig. S8). Further analyzing the fcc/ L_{12} domains (the tip in Fig. 2C), the iso-composition surfaces of 30 at % Fe and 18 at % V were reconstructed in Fig. 2E to reveal the morphologies of L_{12} and fcc phases, respectively. Figure 2F presents a one-dimensional concentration profile from L_{12} to fcc and then to L_{12} . Comparatively speaking, the fcc domain is substantially enriched in Fe but slightly depleted in V and Co. The chemical compositions of fcc matrix and L_{12} phase are $\text{Ni}_{36.8}\text{Co}_{16.4}\text{Fe}_{31.3}\text{V}_{15.5}$ and $\text{Ni}_{37.3}\text{Co}_{18.7}\text{Fe}_{24.4}\text{V}_{19.6}$ (at %), respectively. This L_{12} phase has only ~20 at % V occupying the B site, indicative of a small presence of Co, Fe, or Ni occupying the B site to maintain the ordered structure. The gradual reduction of Fe content from disordered fcc to ordered L_{12} and then to ordered κ implies that the strong interaction among Co, Ni, and V results in the precipitation of the hierarchical LRO phases.

Mechanical properties

The representative room temperature tensile engineering stress-strain curves for the HT, CR, RA, and RAA alloys are presented in Fig. 3A. The repetitive tensile curves are shown in fig. S9. The HT

alloy has a high fracture elongation of 57% but a very low yield strength of 285 MPa. Subsequent severe plastic deformation elevates the yield strength to 1.44 GPa but dramatically reduces the tensile elongation to 7% in the CR alloy due to the limited strain hardening capability. In contrast, the annealed RA alloy achieves a decent fracture elongation of 32% while maintaining a high yield strength of ~1 GPa and a UTS of 1.27 GPa. Following further aging, the RAA alloy attains an ultrahigh UTS of 1.63 GPa along with a remarkable elongation of 30%. Ductile fracture morphology with numerous fine dimples indicates the inherently ductile nature of the RAA alloy (fig. S10). This enhancement in strength coupled with retained ductility after aging benefits from extra strain hardening. Figure 3B shows a larger strain hardening rate ($\Theta = d\sigma/d\varepsilon$, where σ and ε denote true stress and true strain, respectively) and a distinct three-stage behavior with a momentary up-turn in the RAA alloy, as opposed to the monotonic two-stage decrease in the RA alloy. This enhanced and extra strain hardening capability can postpone necking instability while improving the strength (30). Moreover, it is noteworthy that the RAA alloy simultaneously enhances UTS and ductility compared to the CR alloy, thereby breaking the conventional strength-ductility trade-off. Figure 3 (C and D) illustrates the

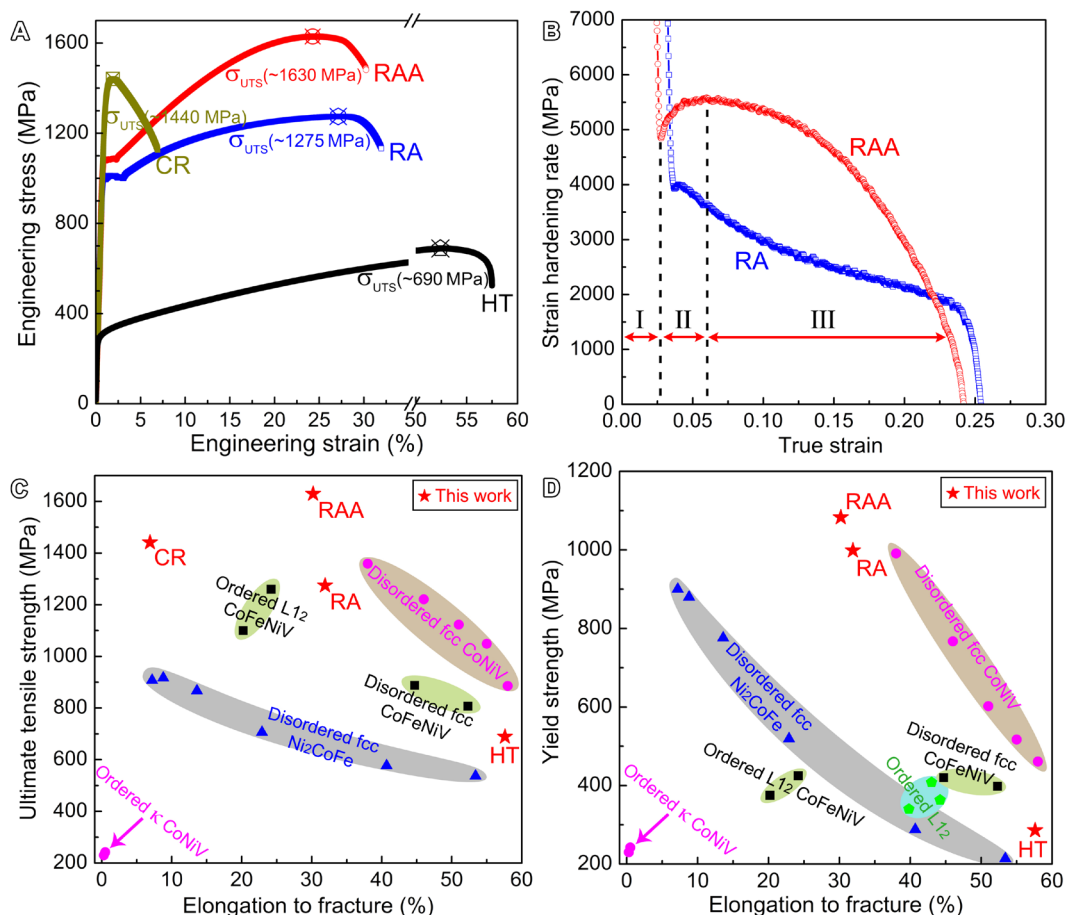


Fig. 3. Mechanical properties of the Ni_2CoFeV MEAs prepared by different processes. (A) Tensile engineering stress-strain curves of the HT, CR, RA, and RAA samples at room temperature. (B) Strain hardening rate versus true strain showing a monotonic two-stage decrease in the RA alloy but a distinct three-stage behavior with a momentary up-turn in the RAA alloy. Comparison of (C) UTS and (D) yield strength versus elongation of our MEAs (red stars) with literature-reported data of the Co-Fe-Ni-V MEA systems (19, 22, 23, 28-30), indicating the optimal strength-ductility combination of tri-phase RAA MEA.

optimal strength and ductility combination achieved by the tri-phase RAA alloy in the Co-Fe-Ni-V MEA system. Besides, this Ni₂CoFeV MEA offers a low-cost advantage over equimolar CoNiV and CoFeNiV MEAs, due to the reduced content of expensive Co and V alloying elements. It is evident that the ductility decreases dramatically after a complete disorder-to-order transition and even becomes brittle for the same alloy composition (25, 26, 31, 32). Although the L₁₂-type intermetallic alloys exhibit high UTSs exceeding 1 GPa, the yield strengths are lower than 430 MPa (25, 32). The RAA alloy, featuring hierarchical ordered phases, is both ductile and strong, showcasing superior strength-ductility synergy compared to most previously reported HEAs/MEAs (fig. S11).

Deformation mechanisms

To investigate the deformation mechanisms, TEM observations were conducted on the tensile-deformed RA and RAA alloys. In the fractured RA alloy, plastic deformation in the fcc grains is dominated by

high-density dislocations, including parallel arrays generated by planar slip and entanglements (Fig. 4, A to C). Moreover, a large number of dislocations pile up at the phase boundaries of κ phase, marked by the yellow arrows in Fig. 4 (A and B), under different two-beam conditions. A few dislocations traverse the κ phase, marked by the green arrows in Fig. 4 (A and B), leading to notable shearing of the κ phase, as shown in Fig. 4C. The retained annealing twins in the fcc grains also hinder dislocation slip.

In contrast, the fractured RAA alloy exhibits an abundance of nano-SF networks in addition to a substantial accumulation of dislocations in the coupled fcc/L₁₂ grains (Fig. 4D). These stored dislocations are a result of simultaneous activation of superlattice dislocations in the ordered L₁₂ domains and conventional unit dislocations in the disordered fcc domains (fig. S12, A to C). Multiple SF bundles are activated on different {111} slip planes at the low strain stage (4%; see fig. S12A) and intersect with each other. A few nano-SF networks are formed at the early stage (fig. S12D). As the strain increases to

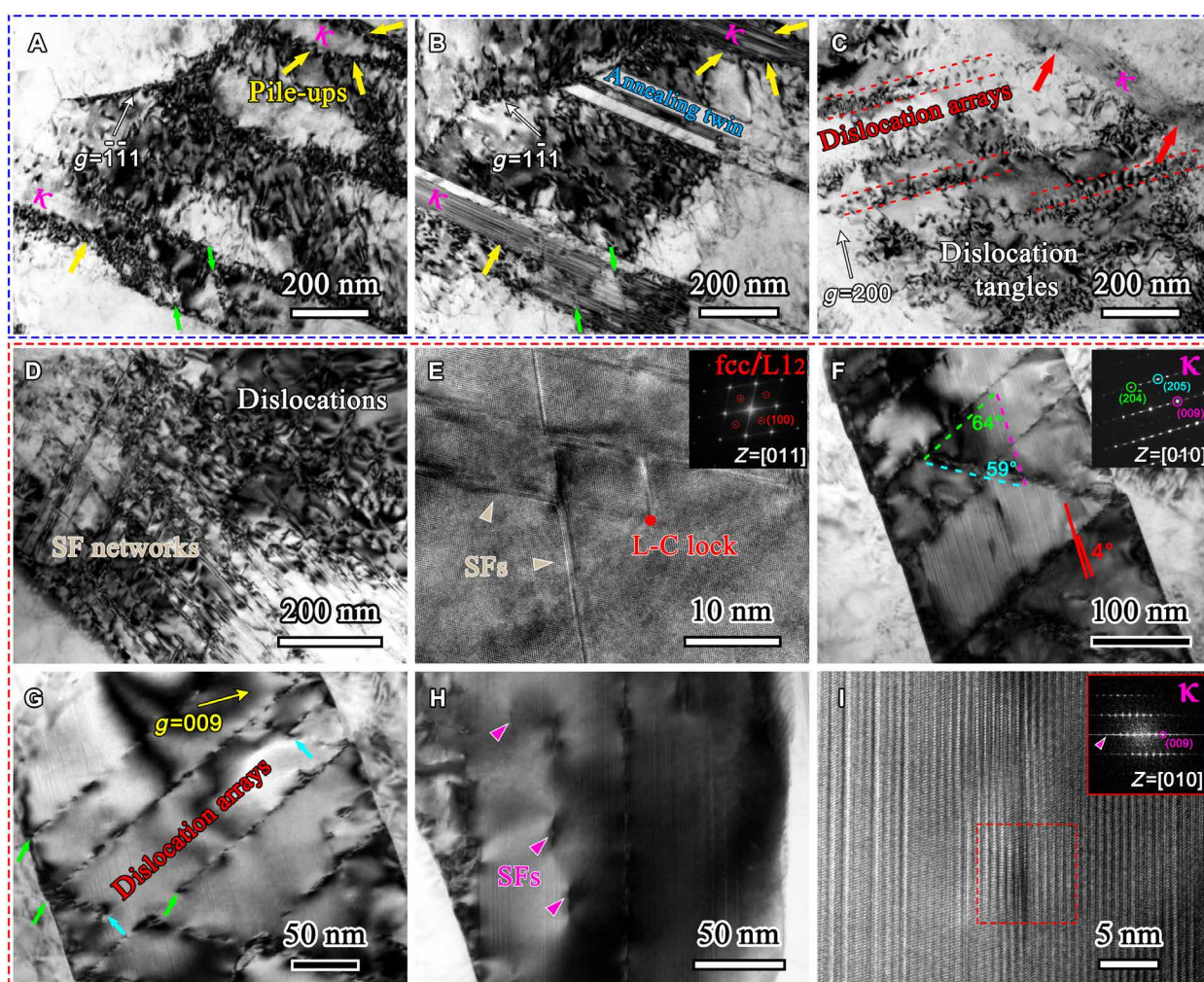


Fig. 4. Deformation microstructures of fractured RA and RAA MEAs after tensile loading. (A to C) Bright-field TEM images of the RA alloy revealing typical dislocation structures in the fcc and κ phases. High-density dislocations pile up at the phase boundaries of the κ phase (marked by yellow arrows), and a few dislocations traverse the κ phase (marked by green arrows), leading to notable shearing of the κ phase (marked by red arrows). (D to I) Bright-field TEM and HRTEM images of the RAA alloy revealing high-density nano-SF networks, dislocations, and L-C locks in the coupled L₁₂ and fcc phases [(D) and (E)] and unusual dislocation multiple slip and SFs in the κ phase [(F) to (I)].

10%, high-density intersecting SFs have been in existence (fig. S12E). When the SFs on different slip planes encounter and interact, the immobile Lomer-Cottrell (L-C) locks are produced (Fig. 4E). Furthermore, high-density dislocations also glide in the κ phase of the RAA alloy and multiple slip is unexpectedly initiated at the later stage (Fig. 4F and fig. S12F). Notably, a low-angle boundary with 4° , formed by dislocation interactions on the primary slip plane, is observed in the κ phase (Fig. 4F). Parallel dislocation arrays on the primary slip planes, marked by the dashed green line, intersect with subsequent dislocations in secondary planes, marked by the dashed blue line. The primary and secondary slip planes are $\{20\cdot4\}$ and $\{205\}$, respectively, and have an angle relationship of $\sim 64^\circ$ and $\sim 59^\circ$ with the $\{009\}$ basal plane. These dislocation structures are clearly visible in the two-beam condition of $g = 009$ (Fig. 4G). In addition, massive deformation-induced SFs with finite lengths are activated in the $\{009\}$ basal planes of the κ phase (Fig. 4H), distinguishing them from annealing-induced SFs. A magnified SF is corroborated by a faint streak in the inserted FFT pattern (Fig. 4I).

DISCUSSION

Here, a Ni_2CoFeV MEA with hierarchical ordered phases is fabricated by straightforward thermomechanical treatment. This MEA has a single-phase fcc structure after high-temperature homogenization, similar to other MEAs in the Co-Fe-Ni-V system (25, 26, 31–34). Direct one-step annealing at intermediate temperatures is commonly used to produce ordered phases, but only one type of precipitate, e.g., the L_{12} phase, formed in the equimolar CoFeNiV MEA (25, 32). In contrast, by applying a two-step annealing process at intermediate temperatures, a stepwise disorder-to-order transition takes place in the Ni_2CoFeV MEA. The occurrence of disorder-to-order transition is assisted by the mixing enthalpy difference between various alloying elements. While Co, Fe, and Ni exhibit close-to-zero mixing enthalpies with each other, V has negative enthalpies with them (35). This can be corroborated by the fact that the equimolar CoFeNi and non-equimolar Ni_2CoFe MEAs remain a single-phase fcc structure after annealing at different temperatures (33, 36). The addition of V to the Co-Fe-Ni system lowers the mixing enthalpy, making the formation of chemical short-range order or even LRO easier, thus reducing the Gibbs free energy (37, 38). Furthermore, depending on the mixing enthalpies, the formation of Ni-V pair has the strongest tendency, while the Fe-V pair is the weakest (35). The Ni-rich environment in the Ni_2CoFeV MEA leads to more nearest-neighbor Ni-V pair rather than Fe-V pair or Co-V pair, promoting the formation of A_3B -type $\text{Ni}_{1.5}(\text{Co, Fe})_{1.5}\text{V}$ ordered phase.

Besides, the occurrence of hierarchical ordering in the Co-Fe-V system is connected with the VEC values ($\text{VEC} = \sum_{i=1}^n x_i \text{VEC}_i$, where x_i is the molar fraction of the different elements and VEC_i for Ni, Co, Fe, and V are 10, 9, 8, and 5, respectively) (22–24). The overall VEC of Ni_2CoFeV MEA is calculated as 8.347, conducive to the formation of κ phase (22). The VEC of κ phase is 8.289 and that of L_{12} phase is 8.345. Abnormally, the VEC of L_{12} phase is higher than that of κ phase, differing from the typical trend where decreasing VEC leads to a crystal structure change from trigonal to hexagonal, and eventually to cubic (22). The overhigh VEC of L_{12} phase in the RAA alloy is attributed to the substitution of V with Co, Fe, or Ni at the B site, due to the insufficient V content with only ~ 20 at %. The composition of L_{12} phase is $(\text{Ni}_2\text{CoFe})_3(\text{V}_4\text{Fe})$ with approximately 5

at % Fe occupying the B site, as confirmed by the density functional theory-calculated formation energies (fig. S13). Analogously, the occupation of Fe atoms at both A and B sites is revealed in other L_{12} -type multicomponent intermetallic nanoparticles, thus reducing the formation energies (10, 39). Therefore, the ingenious composition design and efficient processing technology trigger the unique tri-phase structure composed of disordered fcc and ordered L_{12} and κ phases.

The remarkable strength and ductility combination primarily derives from the crystal structure difference between disordered phase and hierarchical ordered phases. First, the primary contributors to the gigapascal yield strength of the RAA alloy are grain refinement and second-phase (mainly κ phase) strengthening. The strengthening effect of L_{12} phase is relatively subtle, as evidenced by the marginal improvement in yield strength from RA to RAA alloys (only ~ 85 MPa; see Fig. 3A). Likewise, the yield strength of CoFeNiV MEA experiences minimal change after complete disorder-to-order transition from fcc to L_{12} (25, 32). This phenomenon suggests that superlattice dislocations in the ordered L_{12} structure may require no additional stress for glide compared to the ordinary dislocations in the disordered fcc structure. It can be verified that superlattice dislocations and ordinary unit dislocations coexist at the early stage in the RAA alloy (4%; see fig. S12, A to C). Furthermore, the introduction of V element in the fcc matrix induces severe lattice distortion, thereby improving the effectiveness of solid solution strengthening (31). Notably, the strengthening effect of κ phase is comparable to the high concentration of vanadium in the equimolar CoNiV MEA, confirmed by the similar yield strength between the RA alloy and the fine-grained fcc CoNiV MEA (grain size of $\sim 2 \mu\text{m}$) (31).

Second, the exceptional ductility of the RAA alloy is attributed to the activation of multiple deformation mechanisms occurring simultaneously in the triple phases. For the fcc domains, the conventional dislocation planar slip dominates the plastic deformation. In the L_{12} domains, the $1/2\langle 110 \rangle$ superlattice dislocations glide in pairs on $\{111\}$ planes. When the paired superlattice dislocations move, the LRO structure is not destroyed. In addition to dislocation slip, numerous fine SFs are activated on two $\{111\}$ slip systems at the early stage of plastic deformation. These SFs subsequently interact with each other to form nano-SF networks. While the extended SFs efficiently impede the movement of dislocations on slip planes crossing the SF plane, these blocked dislocations can still penetrate through the SFs and continue slipping (fig. S12C). The formation of nano-SF networks causes dynamic grain refinement, resulting in a reduction of dislocation mean free path and promoting dynamic Hall-Petch hardening (40, 41). Even in the fractured RAA alloy, high-density intersecting SFs persist (Fig. 4D), indicative of the enduring hardening effect of the SFs. This dislocation/SF-dominated deformation in the coupled fcc/ L_{12} phases of the RAA alloy differs from the mode of dislocation and deformation-induced microband in the classical L_{12} nanoparticle-strengthened CoFeNi -based MEAs (10, 42). It can be attributed to the lower APB energy of $(\text{Co, Fe, Ni})_3(\text{V, Fe})$ -type L_{12} phase, compared to $(\text{Co, Fe, Ni})_3(\text{Al, Ti, Fe})$ -type and $(\text{Co, Fe, Ni})_3(\text{Ti, V})$ -type L_{12} phases. Moreover, the interaction of leading partials from two SFs on two $\{111\}$ planes forms a stair-rod dislocation known as an L-C lock. These L-C locks serve as robust obstacles to further dislocation motion on the two $\{111\}$ planes, contributing substantially to strain hardening (43). Thus, the strain hardening rate of the RAA alloy exhibits a momentary upturn when $2.7\% < \epsilon < 6\%$ and maintains a high level exceeding 4

GPa when $\epsilon < 17\%$ (Fig. 3B). For the lath-shaped κ phase, the deformation mechanism has been underexplored due to its intrinsic brittleness. When forming a nearly pure κ phase polycrystalline ordered structure, poor ductility and substantially reduced strength are mainly caused by severe intergranular embrittlement (26, 27). However, introducing the κ phase embedded in the fcc matrix can effectively avoid the risk of intergranular failure among the κ grains. By carefully controlling the annealing temperature, a small fraction of κ phase (from 2.3 vol % to 14.2 vol %) is decomposed from the fcc CoNiV MEA (27). A dislocation-controlled shearing mechanism inside the brittle κ phase is conducive to coordinating plastic deformation at the high strain level (27). In the Ni₂CoFeV MEA, the κ phase contains heavy addition of Fe compared to the CoNiV-type κ phase, of which crystal symmetry can be notably changed. In comparison, the κ phase in the RAA alloy exhibits more plentiful deformation mechanisms apart from dislocation-induced shearing on the primary slip planes. Previously unnoticed SFs on {009} basal planes and dislocations on the secondary slip planes are also activated. Such multiple deformation mechanisms inside κ phase serve to alleviate stress concentration at the phase boundary and promote uniform plastic deformation. Therefore, the simultaneous activation of unusual dislocation multiple slip and SFs in the κ phase, along with the interaction between the intersecting SFs and dislocations in the coupled L1₂ and fcc phases, is beneficial for enhanced strain hardening and excellent UTS and ductility.

In conclusion, a strong and ductile Ni₂CoFeV MEA with hierarchical order-strengthening phases is developed. This strategy effectively mitigates intergranular fracture risks in the purely ordered structures. The unique multiple deformation mechanisms contribute to extraordinary strain hardening ability and ductility. Our work provides a strategy for designing high-performance HEAs/MEAs by introducing multiprincipal-element ordered intermetallic phases in a disordered matrix, particularly promising in the Co-Fe-Ni-V system.

MATERIALS AND METHODS

Sample preparation

The bulk Ni₂CoFeV (at %) MEA ingot was prepared using commercial metals (purity >99.95 wt %) by vacuum induction melting under Ar atmosphere. The ingot was re-melted at least four times to ensure chemical homogeneity. The as-cast alloy was processed by multi-directional forging at room temperature and then homogenized at 1150°C for 6 hours. The HT alloy was cut into plates and then cold-rolled with a thickness reduction of ~90% at room temperature, followed by RA at 750°C for 10 min. Finally, the RA alloy was aged at 650°C for 3 hours. All heat-treated samples were rapidly quenched in water.

Microstructural characterization

The phase constitutions were identified by XRD measurements conducted on a Bruker-AXS D8 Advance diffractometer with Cu-K α radiation. The XRD data were collected with the angle of 2 θ from 30° to 90° and a scanning speed of 1° per minute. EBSD measurements were performed on a TESCAN CLARA scanning electron microscope (SEM) equipped with EDS and BSE detectors. The specimens for SEM and EBSD characterization were mechanically polished, followed by electropolishing using an electrolyte containing 90 vol % acetic acid and 10 vol % perchloric acid with a voltage of 30 V at room temperature. TEM and HRTEM/STEM were performed on

a FEI-Tecna G2 20 S-TWIN microscope operating at 200 kV and a Titan G2 60-300 microscope operating at 300 kV, respectively. Before electropolishing, the small pieces with 3 mm in diameter used for TEM observation were sectioned from the tensile specimens, followed by grinding and polishing into thin foils with thicknesses of ~60 μ m. Finally, these TEM samples underwent electropolishing in a twin jet system containing an electrolyte consisting of 10 vol % perchloric acid, 20 vol % glycerol, and 70 vol % methanol at -20°C. APT measurements were performed using a local electrode atom probe (CAMECA LEAP 4000X Si) with an ultraviolet (UV) laser pulse repetition rate of 200 kHz, at a pulsing laser energy of 50 pJ, a target evaporation rate of 0.8%, and a specimen temperature of 40 K. The tip specimens for APT characterization were prepared by a Carl Zeiss Auriga focused ion beam (FIB) SEM.

Tensile testing

The tensile tests were performed using an LTM-20KN testing machine with a constant strain rate of $1 \times 10^{-3} \text{ s}^{-1}$ at room temperature. Flat dog bone-shaped tensile specimens with a gauge cross section of $2.5 \times 1.5 \text{ mm}$ and a length of 10 mm were electrodischarge-machined. A mechanical extensometer was used for all tensile tests. At least three tensile specimens were tested to obtain repeatable experimental results.

Supplementary Materials

This PDF file includes:

Supplementary Text

Figs. S1 to S13

References

REFERENCES AND NOTES

- J. W. Yeh, S. K. Chen, S. J. Lin, J. Y. Gan, T. S. Chin, T. T. Shun, C. H. Tsau, S. Y. Chang, Nanostructured high-entropy alloys with multiple principal elements: Novel alloy design concepts and outcomes. *Adv. Eng. Mater.* **6**, 299–303 (2004).
- E. P. George, D. Raabe, R. O. Ritchie, High-entropy alloys. *Nat. Rev. Mater.* **4**, 515–534 (2019).
- F. Y. Cao, P. Munroe, Z. F. Zhou, Z. H. Xie, Medium entropy alloy CoCrNi coatings: Enhancing hardness and damage tolerance through a nanotwinned structuring. *Surf. Coat. Technol.* **335**, 257–264 (2018).
- J. Moon, E. Tabachnikova, S. Shumilin, T. Hryhorova, Y. Estrin, J. Brechtel, P. K. Liaw, W. Wang, K. A. Dahmen, H. S. Kim, Unraveling the discontinuous plastic flow of a Co-Cr-Fe-Ni-Mo multiprincipal-element alloy at deep cryogenic temperatures. *Phys. Rev. Mater.* **5**, 083601 (2021).
- J. H. Han, Y. Zhang, Z. Y. Sun, Y. F. Zhang, Y. L. Zhao, L. X. Sun, Z. W. Zhang, Enhanced irradiation tolerance of a medium entropy alloy via precipitation and dissolution of nanoprecipitates. *J. Nucl. Mater.* **586**, 154693 (2023).
- B. Cantor, I. T. H. Chang, P. Knight, A. J. B. Vincent, Microstructural development in equiatomic multicomponent alloys. *Mater. Sci. Eng. A* **375–377**, 213–218 (2004).
- B. Gludovatz, A. Hohenwarter, D. Catoor, E. H. Chang, E. P. George, R. O. Ritchie, A fracture-resistant high-entropy alloy for cryogenic applications. *Science* **345**, 1153–1158 (2014).
- W. Li, D. Xie, D. Li, Y. Zhang, Y. Gao, P. K. Liaw, Mechanical behavior of high-entropy alloys. *Prog. Mater. Sci.* **118**, 100777 (2021).
- L. Liu, Y. Zhang, J. Han, X. Wang, W. Jiang, C. T. Liu, Z. Zhang, P. K. Liaw, Nanoprecipitate-strengthened high-entropy alloys. *Adv. Sci.* **8**, 2100870 (2021).
- T. Yang, Y. L. Zhao, Y. Tong, Z. B. Jiao, J. Wei, J. X. Cai, X. D. Han, D. Chen, A. Hu, J. J. Kai, K. Lu, Y. Liu, C. T. Liu, Multicomponent intermetallic nanoparticles and superb mechanical behaviors of complex alloys. *Science* **362**, 933–937 (2018).
- Y. Yang, T. Chen, L. Tan, J. D. Poplawsky, K. An, Y. Wang, G. D. Samolyuk, K. Littrell, A. R. Lupini, A. Borisevich, E. P. George, Bifunctional nanoprecipitates strengthen and ductilize a medium-entropy alloy. *Nature* **595**, 245–249 (2021).
- L. Han, F. Maccari, I. R. S. Filho, N. J. Peter, Y. Wei, B. Gault, O. Gutfleisch, Z. Li, D. Raabe, A mechanically strong and ductile soft magnet with extremely low coercivity. *Nature* **608**, 310–316 (2022).
- R. K. Nutor, Q. Cao, R. Wei, Q. Su, G. Du, X. Wang, F. Li, D. Zhang, J. Jiang, A dual-phase alloy with ultrahigh strength-ductility synergy over a wide temperature range. *Sci. Adv.* **7**, eabi4404 (2021).

14. X. H. Du, W. P. Li, H. T. Chang, T. Yang, G. S. Duan, B. L. Wu, J. C. Huang, F. R. Chen, C. T. Liu, W. S. Chuang, Y. Lu, M. L. Sui, E. W. Huang, Dual heterogeneous structures lead to ultrahigh strength and uniform ductility in a Co-Cr-Ni medium-entropy alloy. *Nat. Commun.* **11**, 2390 (2020).
15. F. He, D. Chen, B. Han, Q. Wu, Z. Wang, S. Wei, D. Wei, J. Wang, C. T. Liu, J. Kai, Design of DO_{22} superlattice with superior strengthening effect in high entropy alloys. *Acta Mater.* **167**, 275–286 (2019).
16. S. S. Sohn, D. G. Kim, Y. H. Jo, A. K. da Silva, W. Lu, A. J. Breen, B. Gault, D. Pong, High-rate superplasticity in an equiatomic medium-entropy VCoNi alloy enabled through dynamic recrystallization of a duplex microstructure of ordered phases. *Acta Mater.* **194**, 106–117 (2020).
17. T. Yang, Y. L. Zhao, W. H. Liu, J. H. Zhu, J. J. Kai, C. T. Liu, Ductilizing brittle high-entropy alloys via tailoring valence electron concentrations of precipitates by controlled elemental partitioning. *Mater. Res. Lett.* **6**, 600–606 (2018).
18. Z. He, Y. Guo, L. Sun, H. Yan, X. Guan, S. Jiang, Y. Shen, W. Yin, X. Zhao, Z. Li, N. Jia, Interstitial-driven local chemical order enables ultrastrong face-centered cubic multicomponent alloys. *Acta Mater.* **243**, 118495 (2023).
19. W. Qi, W. Wang, X. Yang, L. Xie, J. Zhang, D. Li, Y. Zhang, Effect of Zr on phase separation, mechanical and corrosion behavior of heterogeneous $CoCrFeNiZr$ high-entropy alloy. *J. Mater. Sci. Technol.* **109**, 76–85 (2022).
20. S. Guo, C. Ng, J. Lu, C. T. Liu, Effect of valence electron concentration on stability of fcc or bcc phase in high entropy alloys. *J. Appl. Phys.* **109**, 103505 (2011).
21. C. T. Liu, J. O. Stiegler, Ductile ordered intermetallic alloys. *Science* **226**, 636–642 (1984).
22. C. T. Liu, Physical metallurgy and mechanical properties of ductile ordered alloys (Fe, Co, Ni)₃V. *Int. Met. Rev.* **29**, 168–194 (1984).
23. C. T. Liu, Atomic ordering and structural transformation in the V-Co-Ni ternary alloys. *Metall. Trans.* **4**, 1743–1753 (1973).
24. C. T. Liu, H. Inouye, Control of ordered structure and ductility of (Fe, Co, Ni)₃V alloys. *Metall. Trans. A* **10**, 1515–1525 (1979).
25. S. Wang, S. Chen, Y. Jia, Z. Hu, H. Huang, Z. Yang, A. Dong, G. Zhu, D. Wang, D. Shu, F. Tian, Y. Dai, B. Sun, FCC-L₁₂ ordering transformation in equimolar FeCoNiV multi-principal element alloy. *Mater. Des.* **168**, 107648 (2019).
26. J. Tian, K. Tang, Y. K. Wu, T. H. Cao, J. B. Pang, F. Jiang, Effects of Al alloying on microstructure and mechanical properties of VCoNi medium entropy alloy. *Mater. Sci. Eng. A* **811**, 141054 (2021).
27. F. An, J. Hou, J. Liu, B. Qian, W. Lu, Deformable κ phase induced deformation twins in a CoNiV medium entropy alloy. *Int. J. Plast.* **160**, 103509 (2023).
28. X. H. An, M. Song, Y. Huang, X. Z. Liao, S. P. Ringer, T. G. Langdon, Y. T. Zhu, Twinning via the motion of incoherent twin boundaries nucleated at grain boundaries in a nanocrystalline Cu alloy. *Scr. Mater.* **72–73**, 35–38 (2014).
29. T. Takasugi, O. Izumi, Deformation of CoTi polycrystals. *J. Mater. Sci.* **23**, 1265–1273 (1988).
30. L. Gu, A. Meng, X. Chen, Y. Zhao, Simultaneously enhancing strength and ductility of HCP titanium via multi-modal grain induced extra $\langle c+a \rangle$ dislocation hardening. *Acta Mater.* **252**, 118949 (2023).
31. S. S. Sohn, A. K. da Silva, Y. Ikeda, F. Kormann, W. Lu, W. S. Choi, B. Gault, D. Pong, J. Neugebauer, D. Raabe, Ultrastrong medium-entropy single-phase alloys designed via severe lattice distortion. *Adv. Mater.* **31**, e1807142 (2019).
32. Z. Ye, C. Li, M. Zheng, X. Zhang, X. Yang, J. Gu, In situ EBSD/DIC-based investigation of deformation and fracture mechanism in FCC- and L₁₂-structured FeCoNiV high-entropy alloys. *Int. J. Plast.* **152**, 103247 (2022).
33. L. Gu, N. Liang, D. Zhang, Y. Fan, J. Liu, Y. Zhao, Tailoring microstructure of Ni₂CoFe medium-entropy alloy to achieve optimal comprehensive mechanical properties. *J. Mater. Res. Technol.* **23**, 4258–4267 (2023).
34. L. Gu, R. Hou, Y. Liu, G. Chen, J. Liu, G. Zheng, R. Zhang, Y. Zhao, Strengthening and toughening bulk Ni₂CoFeV_{0.5} medium-entropy alloy via thermo-mechanical treatment. *J. Mater. Sci. Technol.* **151**, 19–29 (2023).
35. A. Takeuchi, A. Inoue, Classification of bulk metallic glasses by atomic size difference, heat of mixing and period of constituent elements and its application to characterization of the Main alloying element. *Mater. Trans.* **46**, 2817–2829 (2005).
36. X. L. An, H. Zhao, C. L. Chu, T. Dai, T. Lu, Z. H. Huang, C. Guo, P. K. Chu, Hall-Petch relationship and corrosion behavior of cold-rolled CoNiFe medium entropy alloy. *J. Alloys Compd.* **807**, 151698 (2019).
37. Y. Zhang, T. T. Zuo, Z. Tang, M. C. Gao, K. A. Dahmen, P. K. Liaw, Z. P. Lu, Microstructures and properties of high-entropy alloys. *Prog. Mater. Sci.* **61**, 1–93 (2014).
38. X. Chen, Q. Wang, Z. Cheng, M. Zhu, H. Zhou, P. Jiang, L. Zhou, Q. Xue, F. Yuan, J. Zhu, X. Wu, E. Ma, Direct observation of chemical short-range order in a medium-entropy alloy. *Nature* **592**, 712–716 (2021).
39. L. Liu, Y. Zhang, J. Li, M. Fan, X. Wang, G. Wu, Z. Yang, J. Luan, Z. Jiao, C. T. Liu, P. K. Liaw, Z. Zhang, Enhanced strength-ductility synergy via novel bifunctional nano-precipitates in a high-entropy alloy. *Int. J. Plast.* **153**, 103235 (2022).
40. T. Yang, Y. L. Zhao, J. H. Luan, B. Han, J. Wei, J. J. Kai, C. T. Liu, Nanoparticles-strengthened high-entropy alloys for cryogenic applications showing an exceptional strength-ductility synergy. *Scr. Mater.* **164**, 30–35 (2019).
41. Q. Pan, M. Yang, R. Feng, A. C. Chuang, K. An, P. K. Liaw, X. Wu, N. Tao, L. Lu, Atomic faulting induced exceptional cryogenic strain hardening in gradient cell-structured alloy. *Science* **382**, 185–190 (2023).
42. L. Wang, X. Wu, H. Su, B. Deng, G. Liu, Z. Han, Y. Su, Y. Huang, Y. Zhang, J. Shen, G. Zhang, Microstructure and mechanical property of novel L₁₂ nanoparticles-strengthened CoFeNi-based medium entropy alloys. *Mater. Sci. Eng. A* **840**, 142917 (2022).
43. X. D. Xu, P. Liu, Z. Tang, A. Hirata, S. X. Song, T. G. Nieh, P. K. Liaw, C. T. Liu, M. W. Chen, Transmission electron microscopy characterization of dislocation structure in a face-centered cubic high-entropy alloy Al_{0.1}CoCrFeNi. *Acta Mater.* **144**, 107–115 (2018).
44. A. Zunger, S. H. Wei, L. G. Ferreira, J. E. Bernard, Special quasirandom structures. *Phys. Rev. Lett.* **65**, 353–356 (1990).
45. A. V. D. Walle, M. Asta, G. Ceder, The alloy theoretic automated toolkit: A user guide. *Calphad* **26**, 539–553 (2002).
46. A. V. D. Walle, Multicomponent multisublattice alloys, nonconfigurational entropy and other additions to the Alloy Theoretic Automated Toolkit. *Calphad* **33**, 266–278 (2009).
47. G. Kresse, J. Furthmüller, Efficient iterative schemes for ab initio total-energy calculations using a plane-wave basis set. *Phys. Rev. B* **54**, 11169–11186 (1996).
48. J. P. Perdew, K. Burke, M. Ernzerhof, Generalized gradient approximation made simple. *Phys. Rev. Lett.* **77**, 3865–3868 (1996).
49. G. Kresse, D. Joubert, From ultrasoft pseudopotentials to the projector augmented-wave method. *Phys. Rev. B* **59**, 1758–1775 (1999).
50. H. Chung, D. W. Kim, W. J. Cho, H. N. Han, Y. Ikeda, S. Ishibashi, F. Körmann, S. S. Sohn, Effect of solid-solution strengthening on deformation mechanisms and strain hardening in medium-entropy V_{1-x}Cr_xCoNi alloys. *J. Mater. Sci. Technol.* **108**, 270–280 (2022).
51. F. J. Guo, Y. F. Wang, M. S. Wang, W. Wei, Q. He, Q. Y. Wang, C. X. Huang, R. R. Jin, The critical grain size for optimal strength-ductility synergy in CrCoNi medium entropy alloy. *Scr. Mater.* **218**, 114808 (2022).
52. Y. Wang, X. Ma, F. Guo, Z. Zhao, C. Huang, Y. Zhu, Y. Wei, Strong and ductile CrCoNi medium-entropy alloy via dispersed heterostructure. *Mater. Des.* **225**, 111593 (2023).
53. M. Yang, D. Yan, F. Yuan, P. Jiang, E. Ma, X. Wu, Dynamically reinforced heterogeneous grain structure prolongs ductility in a medium-entropy alloy with gigapascal yield strength. *Proc. Natl. Acad. Sci. U.S.A.* **115**, 7224–7229 (2018).
54. M. S. Mehranpour, H. Shahmir, M. Nili-ahmadabadi, CoCrFeNiMn high entropy alloy microstructure and mechanical properties after severe cold shape rolling and annealing. *Mater. Sci. Eng. A* **793**, 139884 (2020).
55. Y. Wu, S. Liu, K. Luo, C. Kong, H. Yu, Deformation mechanism and mechanical properties of a CoCrFeNi high-entropy alloy via room-temperature rolling, cryorolling, and asymmetric cryorolling. *J. Alloys Compd.* **960**, 170883 (2023).
56. Z. Chen, H. Xie, H. Yan, X. Pang, Y. Wang, G. Wu, L. Zhang, H. Tang, B. Gao, B. Yang, Y. Tian, H. Gou, G. Qin, Towards ultrastrong and ductile medium-entropy alloy through dual-phase ultrafine-grained architecture. *J. Mater. Sci. Technol.* **126**, 228–236 (2022).
57. Z. Ye, C. Li, M. Zheng, X. Zhang, X. Yang, Q. Wang, J. Gu, Realizing superior strength-ductility combination in dual-phase AlFeCoNiV high-entropy alloy through composition and microstructure design. *Mater. Res. Lett.* **10**, 736–743 (2022).
58. S. J. Sun, Y. Z. Tian, H. R. Lin, X. G. Dong, Y. H. Wang, Z. J. Zhang, Z. F. Zhang, Enhanced strength and ductility of bulk CoCrFeMnNi high entropy alloy having fully recrystallized ultrafine-grained structure. *Mater. Des.* **133**, 122–127 (2017).
59. T. J. Jang, W. S. Choi, D. W. Kim, G. Choi, H. Jun, A. Ferrari, F. Körmann, P. Choi, S. S. Sohn, Shear band-driven precipitate dispersion for ultrastrong ductile medium-entropy alloys. *Nat. Commun.* **12**, 4703 (2021).
60. J. He, S. K. Makineni, W. Lu, Y. Shang, Z. Lu, Z. Li, B. Gault, On the formation of hierarchical microstructure in a Mo-doped NiCoCr medium-entropy alloy with enhanced strength-ductility synergy. *Scr. Mater.* **175**, 1–6 (2020).
61. W. H. Liu, Z. P. Lu, J. Y. He, J. H. Luan, Z. J. Wang, B. Liu, Y. Liu, M. W. Chen, C. T. Liu, Ductile CoCrFeNiMo_x high entropy alloys strengthened by hard intermetallic phases. *Acta Mater.* **116**, 332–342 (2016).
62. R. Fan, L. Wang, L. Zhao, L. Wang, S. Zhao, Y. Zhang, B. Cui, Synergistic effect of Nb and Mo alloying on the microstructure and mechanical properties of CoCrFeNi high entropy alloy. *Mater. Sci. Eng. A* **829**, 142153 (2022).
63. W. Jiang, H. Wang, Z. Li, Y. Zhao, Enhanced mechanical properties of a carbon and nitrogen co-doped interstitial high-entropy alloy via tuning ultrafine-grained microstructures. *J. Mater. Sci. Technol.* **144**, 128–137 (2023).
64. X. Liu, M. Zhang, Y. Ma, W. Dong, R. Li, Y. Lu, Y. Zhang, P. Yu, Y. Gao, G. Li, Achieving ultrahigh strength in CoCrNi-based medium-entropy alloys with synergistic strengthening effect. *Mater. Sci. Eng. A* **776**, 139028 (2020).
65. H. Chang, T. W. Zhang, S. G. Ma, D. Zhao, T. X. Bai, K. Wang, Z. Q. Li, Z. H. Wang, Strengthening and strain hardening mechanisms in precipitation-hardened CrCoNi medium entropy alloys. *J. Alloys Compd.* **896**, 162962 (2022).

66. D. D. Zhang, J. Y. Zhang, J. Kuang, G. Liu, J. Sun, Low modulus-yet-hard, deformable multicomponent fibrous B2-phase making a medium-entropy alloy ultra-strong and ductile. *Scr. Mater.* **222**, 115058 (2023).

Acknowledgments: We acknowledge the support of the Jiangsu Key Laboratory of Advanced Micro-Nano Materials and Technology. SEM, TEM, and EBSD experiments are performed at the Materials Characterization and Research Center of Nanjing University of Science and Technology. **Funding:** Y.Z. and X.C. acknowledge financial supports from the National Key R&D Program of China (grant no. 2021YFA1200203), National Natural Science Foundation of China (grant nos. 92366201, 51971112, 51225102, and 52371068), and Jiangsu Province Leading Edge Technology Basic Research Major Project (BK20222014). **Author contributions:** L.G. designed the project and wrote the draft manuscript. L.G. and R.H. prepared the alloys. L.G.

performed tensile tests. L.G., Y.L., F.L., and R.Z. performed TEM measurements. L.G. and B.Z. performed SEM and EBSD measurements. Y. Wu performed APT measurements. Y.F. performed first-principles calculations. L.G. and N.L. performed FIB measurements. L.G., Y.L., Y. Wu, Y.C., G.S., G.C., Y. Wang, X.C., and Y.Z. analyzed the data. X.C. and Y.Z. supervised the project and revised the manuscript. All authors contributed to the discussion of the results and comments on the manuscript. **Competing interests:** The authors declare that they have no competing interests. **Data and materials availability:** All data needed to evaluate the conclusions in the paper are present in the paper and/or the Supplementary Materials.

Submitted 27 December 2023

Accepted 24 April 2024

Published 29 May 2024

10.1126/sciadv.adn7553